Arabian Journal for Science and Engineering
https://doi.org/10.1007/s13369-025-10177-y

RESEARCH ARTICLE-MECHANICAL ENGINEERING

Influence of Microstructure Changes on the Stress Corrosion Properties of U-bend S275 Mild Steel

Shahid Parapurath[1] · **Liya Jacob**[1,2] · **Nader Vahdati**[3] · **Ebru Gunister**[4]

Received: 6 January 2025 / Accepted: 17 March 2025

Abstract

Current research investigates the material degradation behavior of thermally processed S275 mild steel under continuous stress in chloride and sulfate media at different pH values (4, 7, and 10). The mild steel samples were quenched at 1000 °C, followed by tempering at 600 °C, followed by U-bending the samples and attaching a bolt and nut to develop continuous stress according to ASTM standards. A U-bend sample without heat treatment was used as a reference. The corrosion behavior of the samples was evaluated using linear polarization resistance and potentiodynamic polarization scans. Optical microscopy, scanning electron microscope, roughness measurements, and Raman spectroscopy have been used to examine the wear behavior of S275 samples. Quenching followed by tempering caused the quasi-polygonal ferrite and granular bainite to convert to martensite. This microstructural change impacted on the material's mechanical properties and corrosion behavior. Tempering caused a 38% increase in ultimate tensile strength and a 103% increase in yield strength. It also caused a 7–27% increase in corrosion resistance in sulfate media. The pH of the electrolyte solution also influenced corrosion. The corrosion rate of the original and tempered U-bend samples in acidic sulfate media showed approximately a 700% increase in corrosion rate compared to media alkaline and neutral sulfate media samples. The prime reason for the exponential increase in the corrosion rate is the effect of the chemical reaction of highly oxidative species on stress-induced surface defects. Raman analysis confirmed a variety of ferrous oxides and hydroxide formations on the surface of S275 steel.

Keywords Stress-induced corrosion · Heat treatment · Potential of hydrogen (pH) · Electrochemical corrosion · Material properties

1 Introduction

Steel is an alloy of carbon and iron. In the production of steel, carbon plays a critical role as a primary element for hardening and strengthening the material. Other additives provide properties like tensile strength, hardness, corrosion resistance, malleability, durability, etc. Excellent mechanical properties and low cost make them suitable for various applications [1–4]. Different types of steel are selected based on their properties for applications. Based on the steel's production technique and carbon content, steels are classified into mild steel, medium steel, and high-carbon steel. Mild steel is regularly employed in the oil, gas, and petroleum industries in construction, drilling, and structures [5–7].

The mild steel S275 series, consisting of S275J0, S275J2, and S275JR, finds extensive use in various structural applications due to its varying impact toughness properties. S275JR, tested at 20 °C, ensures a minimum impact energy of 27 J, while S275 J0, tested at 0 °C, offers enhanced toughness for colder environments. S275J2, tested at − 20 °C, provides the highest impact resistance, making it suitable for even more demanding low-temperature conditions. Their exceptional mechanical and welding characteristics, machinability,

---

✉ Nader Vahdati
nader.vahdati@ku.ac.ae

[1] Department of Mechanical and Nuclear Engineering, Khalifa University of Science and Technology, P.O. Box 127788, Abu Dhabi, United Arab Emirates

[2] Department of Materials Science and Engineering, Norwegian University of Science and Technology (NTNU), 7491 Trondheim, Norway

[3] Department of Mechanical and Nuclear Engineering, Healthcare Engineering Innovation Group, Khalifa University of Science and Technology, P.O. Box 127788, Abu Dhabi, United Arab Emirates

[4] Department of Mechanical Engineering, Faculty of Engineering and Natural Sciences, Istanbul Health and Technology University, 34445 Istanbul, Turkey

and high strength render them valuable in the construction of frames, brackets, joint supports, and vehicle components, as well as for general maintenance across several industries, including oil and gas, automotive, and aeronautical. S275 does not contain large amounts of chromium or nickel, which makes them prone to corrosion. Different researchers have studied the corrosion behavior of S275 steel. Gassama et al. [8] studied the corrosion of unaltered S275 steel using a simulated marine environment and found that S275 shows poor corrosion resistance. The higher proportion of FeO_x and a lower proportion of Fe^{2+} oxides result in the formation of a thin passive film, which results in the material's corrosion. Passive films are usually formed on the metal's surface in contact with alkaline media and provide anti-corrosion properties. Pulsed eddy currents have been utilized by several researchers [9–11] to investigate the corrosion properties of S275. They used this technique to study the effectiveness of different coating techniques for corrosion resistance.

Corrosion results in the formation of iron hydroxides (α-FeOOH: goethite, Fe(OH): ferric hydroxide, ferrous hydroxide, $Fe(OH)_3$); iron oxides (γ-Fe_2O_3: maghemite, α-Fe_2O_3: hematite and Fe_3O_4: magnetite), chlorides (ferric chloride $FeCl_3$ and ferrous chloride $FeCl_2$), and on mild steel depending on their environment. Depending on the stages of corrosion and environmental factors like pH, temperature, and chemicals, the corrosion mechanism varies. The microstructure and stress on the steel also play a crucial role in these interactions, as even slight changes in microstructure can result in different corrosion rates and mechanisms [12]. Selecting the appropriate type of steel is essential for structural applications, as corrosion rate varies by steel type.

Heat treatment refers to a series of metalworking techniques, including annealing, tempering, hardening, and normalizing, to modify a material's physical and/or chemical properties. These processes are utilized to enhance various steel properties, including tensile strength, hardness, Young's modulus, ductility, and corrosion resistance. Heat treatment and microstructure can significantly affect corrosion behavior. Silva et al. [13] studied the influence of microstructural differences on thermally aged duplex steels on corrosion. The sigma transformation of the steel's phase structure reduced the effect of corrosion. Isfahani et al. [14] studied the effect of heat treatment on the corrosion of AISI420 steel and reported that the corrosion behavior changes according to the austenitizing temperature due to the dissolved chromium and carbon in the steel. Majumdar et al. [15] used laser surface melting for the heat treatment of 304L samples and found that the microstructure changes and increased δ-ferrite content with the removal and redistribution of sulfur inclusions helped the corrosion resistance. Amezhnov et al. [16] reported the increased corrosion resistance of mild steel employed in oil and gas pipelines after quenching and tempering heat treatment. Parapurath et al. [17] investigated the material degradation of S275 steel with electrochemical methods. Quenching as a heat treatment method has lowered the steel's corrosion rate by forming a martensitic microstructure. Gupta et al. [18] studied the effect of tempering CO2-induced corrosion resistance and found that tempering at 600 °C significantly reduced corrosion compared to tempering at 300 °C. Ren et al. [19] observed that as the tempering temperature increased, ferrite grains coarsened, average dislocation density decreased, and vanadium carbide size grew while its quantity declined in mild steel with high vanadium content. However, increased interface distortion between vanadium carbide and the matrix raised local dislocation density, reducing corrosion potential and impedance. Consequently, stress corrosion sensitivity worsened. Similar observation was made by Xin et al. [20], where they observed that a higher tempering temperature refines microstructure, enhances toughness, and improves stress corrosion cracking resistance. In general, the microstructure changes and the redistribution or exclusion of inclusions in the steel structure cause better corrosion resistance.

Along with microstructure and chemical environment, another important factor that affects the corrosion behavior is the compressive and tensile stress of the material. In most applications, the steel is bent to different shapes, increasing the stress on specific areas of the sample, which can effectively change the innate corrosion properties. Sheng et al. [21] studied the effect of H-bending on a steel beam in an underground environment and found that the H-bending resulted in the growth of pit and non-uniform corrosion. Labanowski et al. [22] studied the impact of the microstructure of austenitic-ferritic steel on its mechanical properties and susceptibility to stress corrosion cracking. Experiments were performed to study stress corrosion under tension at a low strain rate in both an inert and a corrosive environment. The corrosion resistance of the steel decreases when subjected to an aging temperature of 500 °C, even with minor structural transformations occurring. Structural transformations occurring at 700 °C temperature affect susceptibility to stress corrosion of the steel to a small extent; however, they cause a drastic decrease in its plasticity. This shows the effect stress has on the corrosion properties of different types of steel combined with heat treatment.

Steel structures are frequently exposed to a variety of mechanical stresses, including tensile, compressive and cyclic loads, which arise from external forces such as wind, seismic activity, and operational loads plus residual stresses. This highlights the need for studying the influence of stress on corrosion behavior. At the same time, these structures often operate in environments containing moisture, chemicals, and pollutants, which can accelerate the corrosion process. The combination of different pHs with stress induced by U-bend gives the study a broader platform to compare and identify potential remediation strategies by understanding the mechanism of corrosion under stress. This study investigates how microstructural changes from heat treatment influence corrosion susceptibility in chloride and sulfate media across acidic, neutral, and alkaline conditions. Understanding these interactions is critical for improving the durability and performance of structural materials in corrosive environments. The study's novelty lies in correlating the microstructural transformations by heat treatment with electrochemical corrosion mechanisms, emphasizing the role of stress-induced in accelerating degradation. The findings provide critical insights for optimizing heat treatment processes and developing corrosion mitigation strategies for structural applications in aggressive environments. It also links microstructural transformations from heat treatment to corrosion susceptibility, which offers valuable insights for optimizing heat treatment processes and corrosion prevention strategies in pH-variable industrial and structural applications.

This work studies the combined effect of heat treatment and continuous stress induced by U-bending on the corrosion rate of S275 mild steel. The microstructural changes and strength properties of the U-bend S275 mild steel quenched at 1000 °C and then tempered at 600 °C were investigated using optical microscopy, scanning electron microscopy (SEM) of the fractured surface and tensile strength testing. Both the heat-treated and original samples were bent into a U-shape using a jig and mandrel apparatus. The continuous stress was maintained using a bolt and nut. These samples under constant stress were examined for their corrosion behavior in NaCl and Na_2SO_4 media at different pH. Raman spectroscopy, optical microscopy, and roughness studies were conducted to examine the corrosion products formed. To the best of our knowledge, no research has been conducted on the effect of heat treatment on the microstructure of U-bend mild steel and its influence on corrosion properties in different environments.

2 Materials and Methods

2.1 Materials

The chemical composition of S275 structural mild steel used in this study is given in Table 1. In general, S275 structural mild steel has yield strength, tensile strength, and elongation at 275 MPa, 410 MPa, and 22%, respectively. The samples were cut into 20 mm × 10 mm × 4 mm dimensions for microstructural studies after polishing with Struers abrasive surfaces and lubricants ranging from 9 to 1 nm size.

2.2 Heat Treatment

The material's properties were enhanced through a heat treatment process that was guided by both the isothermal transformation and iron-carbon equilibrium diagrams. The heat treatment routine was followed as given in Fig. 1. In this heat treatment technique, the temperature was raised to 1000 °C at a rate of 10 °C per minute with a dwell time of 45 min, which was followed by quenching in a water bath. The sample material was further tempered to 600 °C with a dwell time of 30 min to recover the ductility and toughness of the material and then air cooled.

2.3 Surface Analysis

Following the heat treatment, the samples were mounted for grinding and polishing. Table 2 outlines the four-stage surface treatment that involved the use of distinct polishing surfaces to get varying levels of grinding and polishing. Following final polishing, a Vickers indenter was used to evaluate the material's capacity to withstand localized forces. Prior to microstructure analysis using Olympus BX51M microscope, the specimens were etched with a Nital solution comprising of 95% ethanol and 5% HNO_3, further cleaned with ethanol, distilled water and air dried.

The samples were cleaned using ethanol and distilled water with air drying after the corrosion testing. The surface morphology and roughness profile were analyzed using Alicona Infinite Focus and Infinite Focus (IF-MeasureSuite) software for corroded samples. Raman spectroscopy measurements were conducted on a Witec Alpha Raman spectrometer using a 532 nm laser beam.

2.4 Tensile Testing and Hardness Measurement

Figure 2 illustrates the preparation of the tensile test specimens in accordance with the ASTM A370 and ASTM E8 standards. All samples were cut longitudinally to the rolling direction. MTS Alliance RF/150 was used for the testing. Exact stress–strain measurements were obtained using an extensometer. According to the standard, the rate of extension was maintained at 5 mm/min. The data were analyzed using MTS Test Works software. After the tensile testing, the fracture surface was analyzed with the help Quanta FEI 250 SEM. Vickers hardness indenter was employed with 5 Kgf pressure (HV5) for analyzing the hardness of the sample after polishing the surface.

2.5 U-bending

To obtain the appropriate U-bend specimens according to ASTM standards, a jig and mandrel were modeled and designed using solid works software, as shown in Fig. 3(a–f).

Table 1 Chemical composition EN10025 S275 Jr

Elements	C	Mn	Si	P	S	Cu	Al	Cr	Ni	Nb	Mo	V	Ti	N	Fe
wt.%	0.134	0.89	0.012	0.012	0.008	0.004	0.042	0.013	0.007	0.001	0.001	0.001	0.002	0.0032	Bal

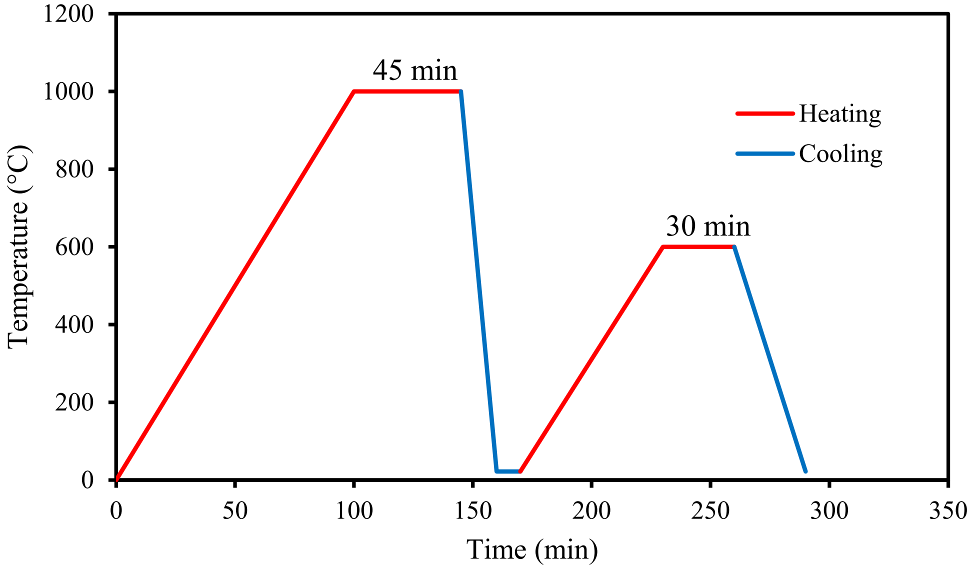

Fig. 1 Schematics illustration of the heat treatment process

Table 2 Parameters for obtaining microstructure after heat treatment

Surface treatment	Abrasive surface	Lubricant	Rate (RPM)	Force and direction
1st stage: Grinding	MD-Primo 220	Water	300	30 N and same direction
2nd stage: Grinding	MD-Allegro	DiaPro Allegro (9 µm)	150	30 N and same direction
3rd stage: Polishing	MD-Mol	DiaPro Mol (3 µm)	150	30 N and same direction
4th stage: Polishing	MD-Chem	OP-S (1 µm)	150	15 N and opposite direction

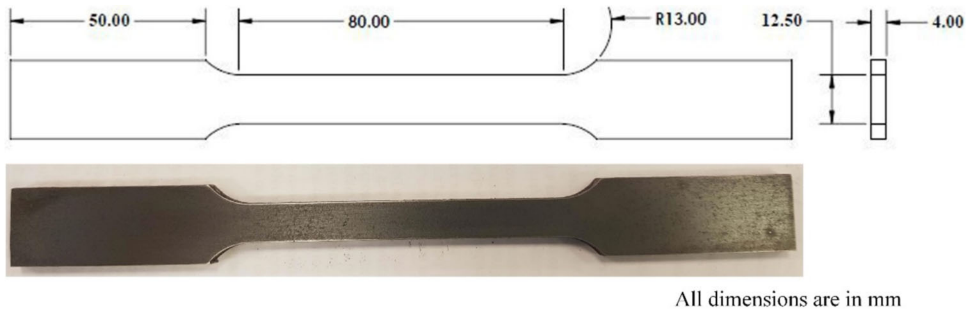

Fig. 2 Sample for tensile testing

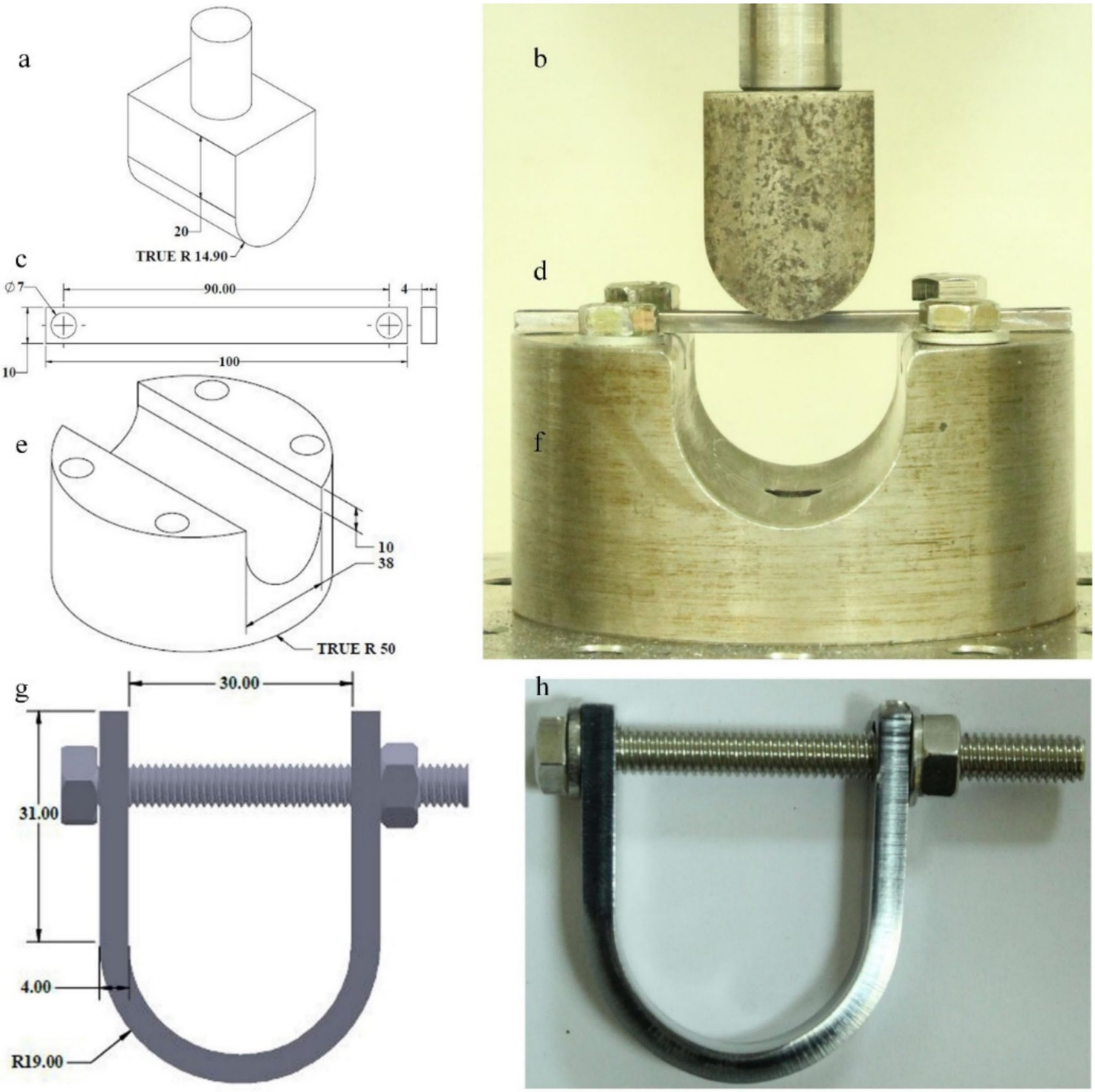

Fig. 3 Jig and mandrel model for preparing U-bend samples (all dimensions are in mm), **a** mandrel, **c** flat sample, **e** jig, **g** schematic of u-bend (solidworks model); **b** mandrel, **d** flat sample, **f** jig, **h** U-bend (machined)

The U-bending of specimens was carried out in accordance with the ASTM standard G30, as shown in Fig. 3(g, h). After the removal of the mandrel from the die, a spring back effect was observed for the samples. The average spring back for the original sample is 8%, and for the tempered sample it is 10%. A bolt and nut were attached to the sample, as given in Fig. 3(g, h), to ensure continuous stress. The U-bend samples with no-heat treatment are referred to as original (O), and the U-bend samples with tempering treatment are called tempered (T) from here on. Corrosion studies were conducted on these samples. All samples were polished from 400 to 1500 grit emery paper in order to maintain surface homogeneity before corrosion testing.

2.6 Electrochemical Measurements

The electrochemical studies were conducted in chloride-free and chloride-rich electrolytes. 3.5% NaCl and 3.5% Na_2SO_4 were used to make neutral (pH 7) chloride and sulfate environment, respectively. Corrosion medium was selected as per

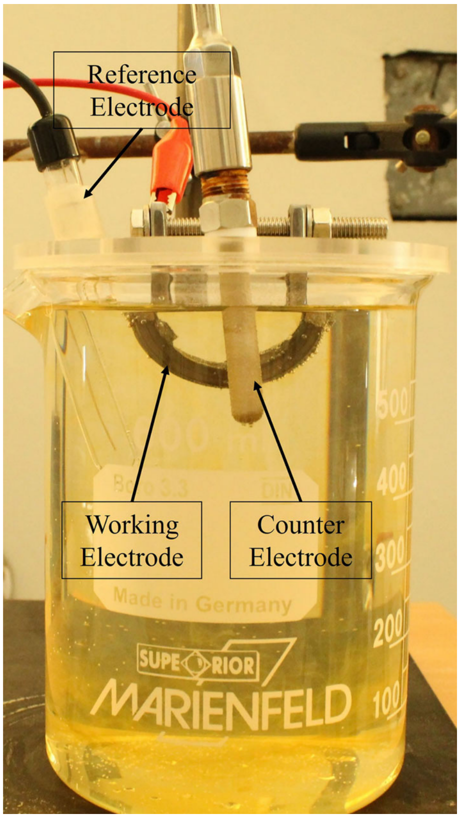

Fig. 4 Three electrode setup for corrosion analysis

ASTM G31 to mimic the real-world conditions. The pH of the solution was modified using drop-by-drop addition of 5% glacial acetic acid to obtain a pH value of 4 and 0.2 M NaOH solution to obtain a pH value of 10 to the respective chloride sulfate environment. A 3-electrode setup was used for conducting the electrochemical tests [23], as given in Fig. 4. Platinum (55 cm^2) and Ag/AgCl were used as the conductive and reference electrodes, respectively. The U-bend S275 sample was attached to the working electrode and dipped in the electrolyte solution with a 6 cm^2 exposed area. To stabilize the system, the open-circuit potential (OCP) was measured for a duration of one hour. Linear polarization rate (LPR) and potentiodynamic polarization were conducted using biologic VMP-300 potentiostat.

The LPR measurements were carried out at a scan rate of 0.1 mV/s, within the potential range of ± 20 mV. The potentiodynamic polarization measurements used a voltage sweeping with a scan rate of 1 mV/s from − 1200 to 800 mV. The anodic and cathodic Tafel constants were calculated using this. The Stern-Geary equation [17, 24] given in Eq. (1) was employed to fit the curve using the EC-lab software. Here, R_p denotes polarization resistance and I_{corr} represents corrosion current density.

$$R_p = \frac{B}{I_{corr}} \tag{1}$$

Constant B is derived from Eq. (2) where β_a and β_b denote the anodic and cathodic constants, respectively.

$$B = \frac{\beta_a \beta_b}{2.3(\beta_a + \beta_b)} \tag{2}$$

Subsequently, the corrosion rate [24] is determined using Eq. (3) with K denoting a constant that corresponds to the units for corrosion rate, E_w representing equivalent weight, D indicating the density and A denoting area of the sample.

$$\text{Corrosion Rate} = \frac{I_{corr}\, K\, E_w}{DA} \tag{3}$$

Twelve different specimens were studied in different heat treatment and corrosion conditions. They were named OC4, OC7, OC10, TC4, TC7, TC10, OS4, OS7, OS10, TS4, TS7, and TS10, where O and T correspond to original and tempered samples, C and S correspond to chloride and sulfate electrolytes, and 4, 7 and 10 denote the pH of the electrolyte media studied. These experiments were repeated thrice, and the average values for Tafel curves were obtained.

3 Results and Discussion

3.1 Microstructure Characterization

From Fig. 5(a), the original sample has quasi-polygonal ferrite (QPF) and granular bainitic ferrite (GBF) as the major phases with pearlite (P), degenerate pearlite (DP), and acicular ferrite (AF) as minor phases distributed throughout the structure. The microstructural classification method, the volume fractions along with the effective grain size, defines QPF, AF, GBF, P, and DP that are crucial in determining the material's susceptibility to corrosion. The sample shows grains in the size of 5–20 µm, with large grains attributing to QPF and small grains attributing to AF. Most grains of AF are high-angled, and their spacing is small. Packets of QPF and GBF have coarse and irregular boundaries with well-developed substructures inside. Coarse packets of GBF are characterized by boundary disorientations. AF is a type of fine ferrite with a needle-shaped morphology, characterized by packets with high-angle boundaries and high-density interior dislocations. These features provide effective resistance against crack cleavage propagation on [100] planes, resulting in a favorable toughness-strength combination. GBF comprises of coarse packets of substructures with parallel low-angle boundaries, along with fine secondary phases present at the

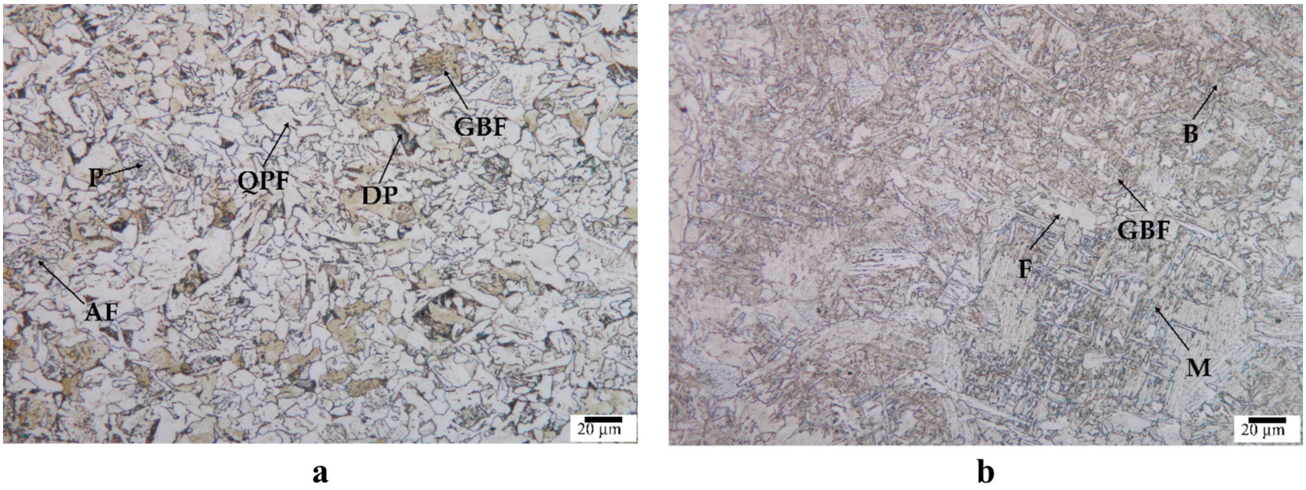

Fig. 5 Microstructure of S275 steel bars prior to U-bending: **a** before heat treatment, **b** after heat treatment

boundaries. Pearlite is composed of ferrite and cementite (Fe_3C) arranged in a lamellar, alternate platelike structure [25]. They are also called hard martensite. The DP phase exhibits a structure that is distinct from a typical P and is referred to as pseudo-pearlite due to the absence of a banding pattern. DP is produced by subjecting the material to slow cooling and normalizing. The rapid cooling rate employed in the accelerated cooling process inhibits the effective diffusion of carbon during cooling, resulting in an inadequate formation of the cementite lamellar structure typically observed in P and promoting the development of DP. Since QPF is generated at a lower temperature and faster cooling rate than the other polygonal ferrites, the shape of its grain becomes irregular [26]. QPFs are distinguished from GBFs because QPFs exhibit minimal development of substructures. Interlocking nature of acicular ferrite that coexists with other ferrite morphologies such as polygonal and quasi-polygonal ferrite, widmastattën ferrite, and allotriomorphic ferrite; acicular ferrite also may grow from inclusions or from another preexisting ferrite plates. The presence of this microstructure is typical in steels used in oil pipelines because it improves their toughness and impact resistance.

During tempering, the main phases in the original samples changed to martensite (M). As shown in Fig. 5(b), the primary phase in the microstructure is martensitic with some delta ferrite (δ-F), alpha ferrite (α-F), GBF, and bainite (B). The presence of GBF and B is scarce. The δ-F is distributed sparsely through the martensitic microstructures with clearly defined grain boundaries. Ferrite crystals are found in iron-carbon alloys body-centered cubic form. Its formation occurs due to the gradual cooling of austenite and the subsequent diffusion of carbon, that begins at 900 °C and carries on till 723 °C [27]. δ-F is a crystalline form of iron which is formed when alloyed steel with low carbon concentrations are cooled from the liquid state before converting into austenite that δ-F can remain stable even at room temperature. When ferrite and cementite grow together, the eutectoid decomposition of austenite occurs through the diffusion of C atoms. Within ferrite laths at the interface, C atoms precipitate as Fe_3C, leading to parallel laths of Fe and Fe_3C, resulting in the construction of δ-F. δ-F is very hard because of the carbon trapped in solid form. The morphology and grain size of the δ-F varies across the samples. Long-banded delta and short-banded delta ferrites were observed, with the size of long-banded delta ferrites measuring 30–40 µm and width of 5–60 µm. No other banded microstructure was observed besides the banded δ ferrites [27]. GBF consists of packets that are relatively coarse in nature inside the island-shaped *M* constituents. They are distinguished by their characteristic brown color. They do not have a clear grain boundary. Most of the GBF seems to be retained from the original sample, which is diffused to the martensitic sites during the transformation. This causes a decrease in fracture toughness as they form sites that initiate crack [28]. Heat-affected steel also has low-volume fractions of sheaf-like bainitic structure with martensite aggregates growing at the grain boundary. This structure was produced by the high cooling rate provided by the quenching, which transforms some austenite and QPF grain into M. This microstructure improves the tensile strength and impact resistance of the steel [29]. In contrast to the decomposition process of ferrite and pearlite, the formation of martensite does not entail atom diffusion. Instead, it happens abruptly through a shear process that does not involve diffusion. For a particular steel, the temperature ranges at which the martensite transformation takes place can be precisely determined. The process of transformation initiates at a martensite start temperature (M_s) and progresses as the temperature drops until the martensite finish temperature (M_f) is achieved. The M_s value varies widely based

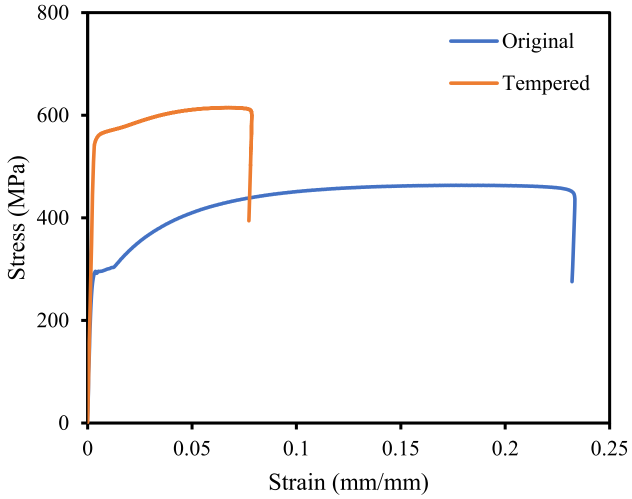

Fig. 6 Engineering stress–strain curve for original and tempered sample before U-bending

on the hardenability of the steel and can range from below room temperature to 500 °C. Generally, the range between M_s and M_f is around 150 °C. In tempered steel, the abundance of martensitic phases with small grain boundaries work to increase the corrosion resistant rate, especially in chloride media [30]. While the corrosion process begins with the formation of a galvanic cell between the anodic ferrite phases and cathodic carbide, the underlying corrosion mechanism varies among different steels with varying microstructures. This can be attributed to the distribution, shape, and size of the galvanic couple.

3.2 Mechanical Properties

Stress–strain curves from the tensile tests on original and tempered samples are illustrated in Fig. 6, Two different types of yielding behavior were observed for the samples. The original sample showed a discontinuous yielding behavior, whereas the tempered sample showed a continuous yielding behavior in their corresponding stress–strain curves [31, 32]. The discontinuous yielding in original samples is due to soft-phase ferrite grains forming low-density dislocation. They also do not have any retained austenite and bainitic transformation in their microstructure that yields continuous stress–strain curves. However, the tempered sample has a continuous stress–strain curve with high-density dislocation by hard phase bainitic and martensitic transformation, which was formed by the cooling process during the heat treatment procedure [31, 32].

Table 3 lists the tensile properties (ultimate tensile strength ($\sigma_{\max}$), Young's modulus (E), yield strength (σ_y), fracture stress (σ_f), and elongation (ε_f)) of the samples. It can be clearly observed that the $\sigma_{\max}$ for tempered samples increased by 38%, and σ_y increased by 103% after heat treatment. This significant increase in strength is due to the presence of martensitic regions after heat treatment (Fig. 5b). However, the elongation percentage has fallen by 69% compared to the original samples, indicating that the heat-treated samples have compromised their ductility. After heat treatment, the martensitic phase of tempered samples causes brittleness. The hard martensitic phase reduces the samples' good formability [32]. The E values remain unchanged.

Table 3 Mechanical properties of original and tempered samples prior to U-bending

Properties	Original (O)	Tempered (T)
$\sigma_{\max}$ (MPa)	445 ± 13.2	615 ± 5.0
E (GPa)	186 ± 6.6	196 ± 10.1
σ_y (MPa)	276 ± 9.9	561 ± 3.0
σ_f (MPa)	285 ± 7.1	394 ± 19.2
ε_f (%)	26 ± 8.3	8 ± 2.2
HV5	137 ± 1.1	221 ± 5.0

Figure 7(a) shows the steel sample before tensile testing. Figure 7(b, c) provides the configurations of failure location for original (O) and tempered (T) samples after the tensile testing procedure. Both the samples clearly displayed a cup and cone formation at the respective fracture area. SEM micrographs of the fractured surface are given in Fig. 7(d–g). Original samples have a uniform dimple fracture pattern seen by the ductile nature of the samples. Tempered samples showed a cleavage-like fracture pattern along with few non-uniform dimples, indicating the brittle nature of the sample [33, 34]. This agrees with the microscopic and tensile strength results.

3.3 Electrochemical Studies

Electrochemical studies were used to understand the corrosion behavior of a material. The Tafel curves of U-bend samples are given in Fig. 8. All samples exhibit diffusion-controlled corrosion behavior as the anodic current density progressively rises with an increase in potential. The corrosion kinetics parameters are determined using Tafel extrapolation. Table 4 provides the corresponding cathodic coefficient (β_c), anodic coefficient (β_a), corrosion current density (I_{corr}), and corrosion potential (E_{corr}) values. All Tafel curves except OS4 and TS4 have similar shapes in anodic and cathodic branches. Distinct corrosion reaction mechanisms are indicated by varying anodic and cathodic Tafel constants for different samples [35]. The corrosion current density is higher for all the samples at pH4. The E_{corr} shifted to higher potential in pH4 (OS4, TS4, OC4, and TC4). The shift is dependent on pH. The shift in cathodic Tafel region is more pronounced at low pH.

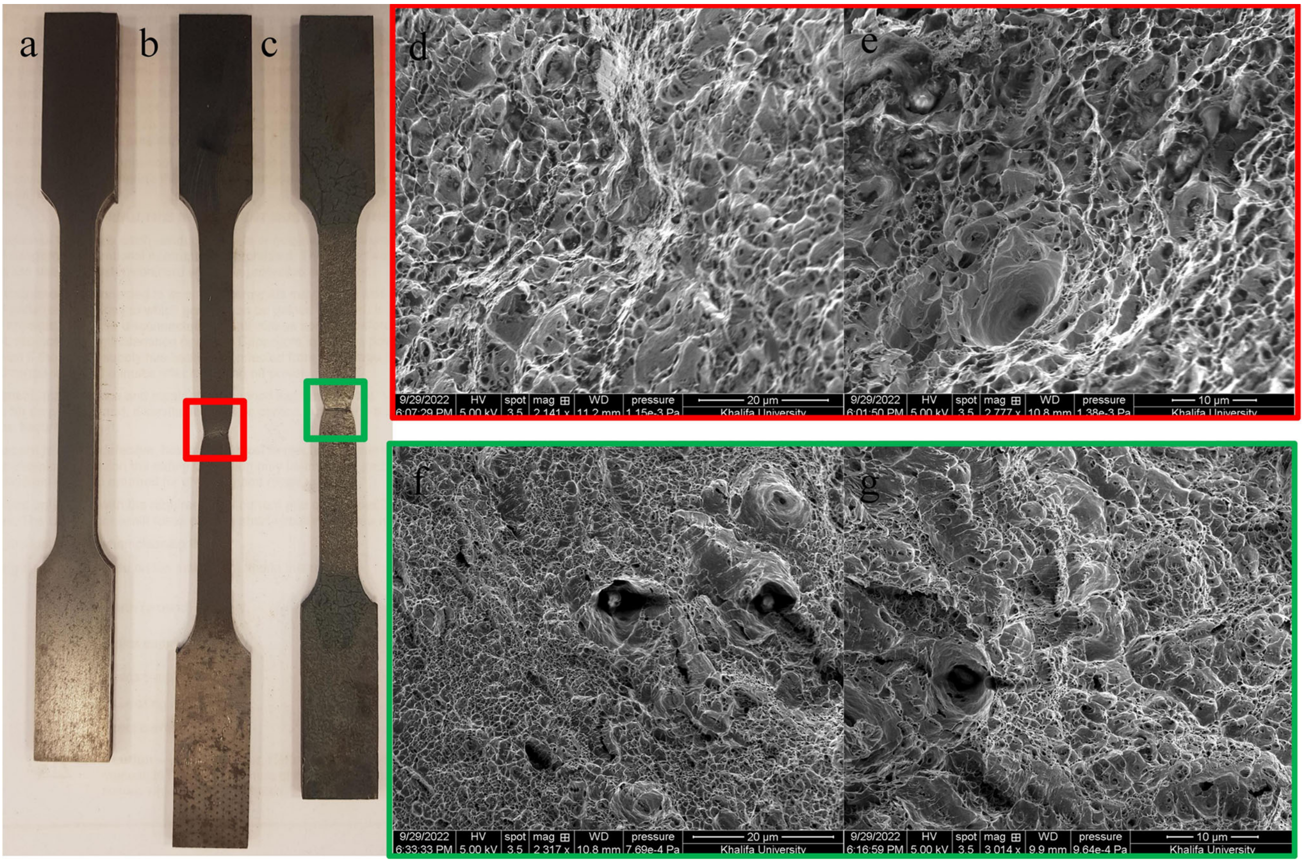

Fig. 7 Fractography of tensile samples; **a** original (*O*) sample before tensile testing, **b** *O* sample after tensile testing, **c** *T* sample after tensile testing, **d** and **e** SEM of *O* sample fractured surface, **f** and **g** SEM of *T* sample fractured surface

I_{corr} is directly proportional to the corrosion current rate [36, 37]. It is found that for the samples in chloride-rich environment, the I_{corr} increased after tempering (TC4, TC7, TC10), showing tempering reduced corrosion resistance. But, for the samples in chloride-free environment, TS4, TS7, and TS10, the corrosion current density decreased after tempering, showing higher corrosion resistance. An iron sulfate film on the metal surface immediately after immersion in the chloride-free environment provided protection, resulting in low corrosion rates for the alkaline samples. In the chloride-rich environment, tempering caused an increase in the corrosion rate. OC4, OC7, and OC10 samples had lower corrosion rates compared to TC4, TC7, and TC10 samples. In the case of the chloride-free environment, TS4, TS7, and TS10 had higher corrosion rates compared to OS4, OS7, and OS10. This might be due to the difference in particle size of chloride and sulfate ions. The martensitic microstructure seems to favor chloride diffusion and absorption [30]. The martensitic tempered steel showed lower cathodic protection against chloride intrusion. The grain boundary precipitation caused by tempering also decreases the cathodic protection against chloride ions. This is explained by the precipitation of chromium carbide at grain boundaries and the consequent decrease in chromium concentration near the boundaries, which promotes chloride corrosion [38, 39].

The lowest corrosion rates in alkaline environments, meaning a rise in pH level, cause a decrease in corrosion rate. The corrosion protectant layer formation was the highest at pH 10. The reason for this was that solutions with low pH levels enhance corrosion by providing hydrogen ions that support oxidation reactions. The presence of chloride ions has a considerable impact on the corrosion in acidic solutions. This is because the chloride ions lead to the breakdown of passivity above a specific potential. Chloride ions slowly penetrate the surface, causing the destruction of the protective film and initiation of corrosion. As observed in Sect. 3.4, chloride corrosion usually results in the uniform pitting of the entire surface of specimens, characterized by flat-bottomed, shallow, and irregularly shaped pits. Chloride penetration is majorly a result of capillary absorption and diffusion in metals.

In the case of sulfate ions, the corrosion rate was comparatively lower for tempered samples. Even then, it follows the same trend with respect to the pH in both the tempered and original samples [40]. In Sect. 3.4, it can be observed that a specimen in a lower pH solution results in fewer but deeper

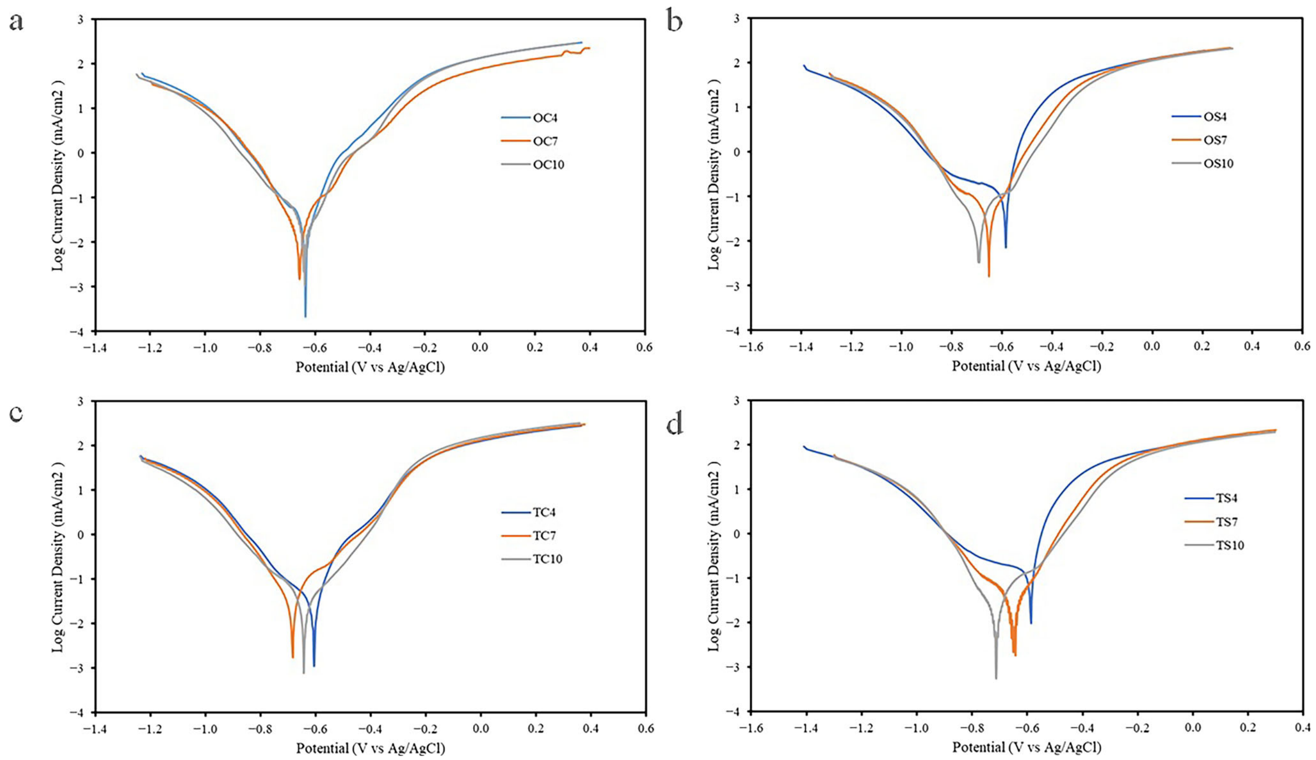

Fig. 8 Tafel curve for samples at pH 4, 7, and 10; **a** and **b** for *O* in chloride and sulfate environment, **c** and **d** for T in chloride and sulfate environment, respectively

Table 4 Potentiodynamic polarization data for original and tempered samples after corrosion

Solution	pH	Sample	E_{corr} (mV)	I_{corr} (μAcm^{-2})	β_{c} (mV)	β_{a} (mV)	R_{p} (ohm)	CR (mmpy)
NaCl	4	OC4	– 636.121	22.706	146.2	99.8	150	0.042
NaCl	7	OC7	– 653.621	19.179	104.8	116.2	156	0.036
NaCl	10	OC10	– 634.453	16.417	114.1	67.3	160	0.031
NaCl	4	TC4	– 630.856	26.023	168	141.4	141	0.049
NaCl	7	TC7	– 687.018	24.137	103.1	95.6	146	0.045
NaCl	10	TC10	– 603.992	18.368	145.6	55.7	157	0.034
Na_2SO_4	4	OS4	– 585.251	139.08	681.8	57.6	39.6	0.260
Na_2SO_4	7	OS7	– 646.191	29.606	174.3	93.5	136	0.055
Na_2SO_4	10	OS10	– 698.827	19.019	111.3	142.8	157	0.036
Na_2SO_4	4	TS4	– 585.995	130.26	536	46	41.9	0.243
Na_2SO_4	7	TS7	– 642.958	21.464	159.9	94.1	135	0.040
Na_2SO_4	10	TS10	– 718.601	16.446	97.6	139	163	0.031

pits, while a specimen in a higher pH solution has more pits with shallow pitting [41].

The presence of residual stress within a material following U-bending serves as a source of activation energy and accelerates the rate of corrosion. The formation of deep grooves during bending gave rise to micro-reaction sites that provide a conducive environment for corrosion. Moreover, corrosion products accumulate at the bottom of these grooves, elevating the continuous evolution of pits. A smooth surface finish can alter the formation of grooves by bending to an extent. U-bending is known to cause stress, plastic deformation, and micro-strains within the material, resulting in changes in surface heterogeneity. These changes are brought about by the fragmentation of grain [42]. It also has a greater interfacial area with the surrounding corrosive environment, influencing the metal surface's susceptibility to the formation of pits [43]. The high corrosion rate in TS4 and OS4 samples was due to the action of sulfate on the stress-induced surface defects of U-bend samples [44]. A previous study conducted [17] on heat-treated straight S275 samples showed similar corrosion values for original and tempered samples in both chloride and sulfate media at different pHs. This indicates that the sharp increase in corrosion rate in TS4 and OS4 stems from the stress-induced U-bending. Compared to other samples, a percentage increase of 600–700% was observed in the acidic sulfate media.

3.4 Corrosion Morphology

The *O* and *T* samples showed different corrosion mechanisms depending on the chemical and acidic environment. The samples showed pitting, intergranular, and uniform corrosion, with the formation of different corrosion products. From Fig. 9 and Fig. S1, OC4 showed uniform corrosion, while TC4 showed pitting with uniform corrosion. The corrosion products in OC4 were deep brown, indicating the presence of hematite distributed throughout the sample. OS4 showed intergranular corrosion with dark gray corrosion products on the grain boundaries, while TS4 had pitting corrosion with large and deep pits. OC7 has general corrosion with a slight occurrence of intergranular corrosion. The small channels might be formed on the cracked regions of the sample as the samples went through U-bend stress. OC7 had milder corrosion compared to OC4, with a small area of uniform corrosion seen in dark brown color. The surface also showed a light-yellow corrosion product. In the case of TC7, a well-distributed channel of intergranular corrosion was observed with slight occurrences of shallow pits. OS7 and TS7 showed pitting corrosion with small and shallow pits, with an average size of 10–50 µm. OC10 showed a mix of intergranular and pitting corrosion. The intergranular corrosion was distributed throughout the structure, and not all were connected. This was due to the induction of corrosion of the cracks of U-bend instead of on the grain boundaries. TC10 showed uniform intergranular corrosion with dark colored corrosion products distributed throughout grain boundaries. OS10 and TS10 also showed a mix of pitting and intergranular corrosion. The intergranular corrosion was distributed throughout the structure in a random order, and the length of the corrosion products varied. The pits were smaller in size and number compared to OS7 and TS7. This agrees well with the electrochemistry results, as the CR was seen as the lowest for all samples in pH 10.

The corrosion mechanism largely depends on the heat treatment, the acidity of the system, and the electrolyte media. The change in acidity and heat treatment causes different surface reactions to occur, resulting in pitting or intergranular corrosion. The process of pitting corrosion in mild steel is a result of the passive film's deterioration, followed by the formation of pits and their subsequent growth [45–47]. The absorption of chloride ions occurs at the surface when they occupy the oxygen ion vacancies. This absorption process involves the vacancy to expand for the larger diameter of the chloride ion, the dehydration of the chloride ion, and the insertion of the chloride ion into the expanded oxygen vacancy. However, this mechanism seemed ineffective in the case of sulfate ions as the size is much larger. The material undergoes uniform/general corrosion in the presence of sulfate ions. Uniform corrosion increases with an increase in acidity, as seen in Fig. 9. When particles containing cathodic elements like manganese and copper are preferentially nucleated and grown at grain boundaries rather than within the grains themselves, solute depletion may occur, resulting in the anodic behavior of grain boundary regions. The content of manganese in S275 makes them prone to forming anodic elements which react easily with the chloride and sulfate from the electrolyte medium. Intergranular corrosion may occur in various alloys, but it is particularly common in heat-treated systems.

The microstructural changes introduced by heat treatment cycle also cause higher corrosion resistance in tempered mild steel. When the main microstructure in mild steel changes from quasi-polygonal ferrite (QPF) and granular bainitic ferrite (GBF) to martensite during heat treatment, corrosion resistance is improved primarily due to alterations in the microstructural features. Martensite formation involves a highly strained lattice structure, leading to a decreased grain size and fewer grain boundaries compared to QPF and GBF. This reduced grain boundary density limits the potential sites for localized corrosion initiation, such as pitting and crevice corrosion. Additionally, martensite's lower carbon content on the surface and higher hardness result in reduced susceptibility to corrosive attack. The transformation also prompts the precipitation of carbides, depleting carbon availability for corrosive reactions. These microstructural changes collectively enhance the material's resistance to corrosion, making tempered martensite more resistant to degradation in corrosive environments [48, 49].

Table 5 gives the surface roughness values of the original and tempered samples after grinding and polishing [5]. The parameters include S_a (arithmetic mean height), which represents the average surface roughness, and S_z (maximum height of the surface), indicating the total height range from peak to valley. Additionally, S_p (maximum peak height) and S_v (maximum pit depth) provide insights into the highest and lowest surface features, respectively. To further analyze the surface characteristics, volumetric parameters such as V_{mp} (peak material volume), V_{mc} (core material volume), V_{vc} (core void volume), and V_{vv} (Valley void volume) have been considered. Both samples showed similar surface roughness before corrosion. This ensures the uniform surface roughness

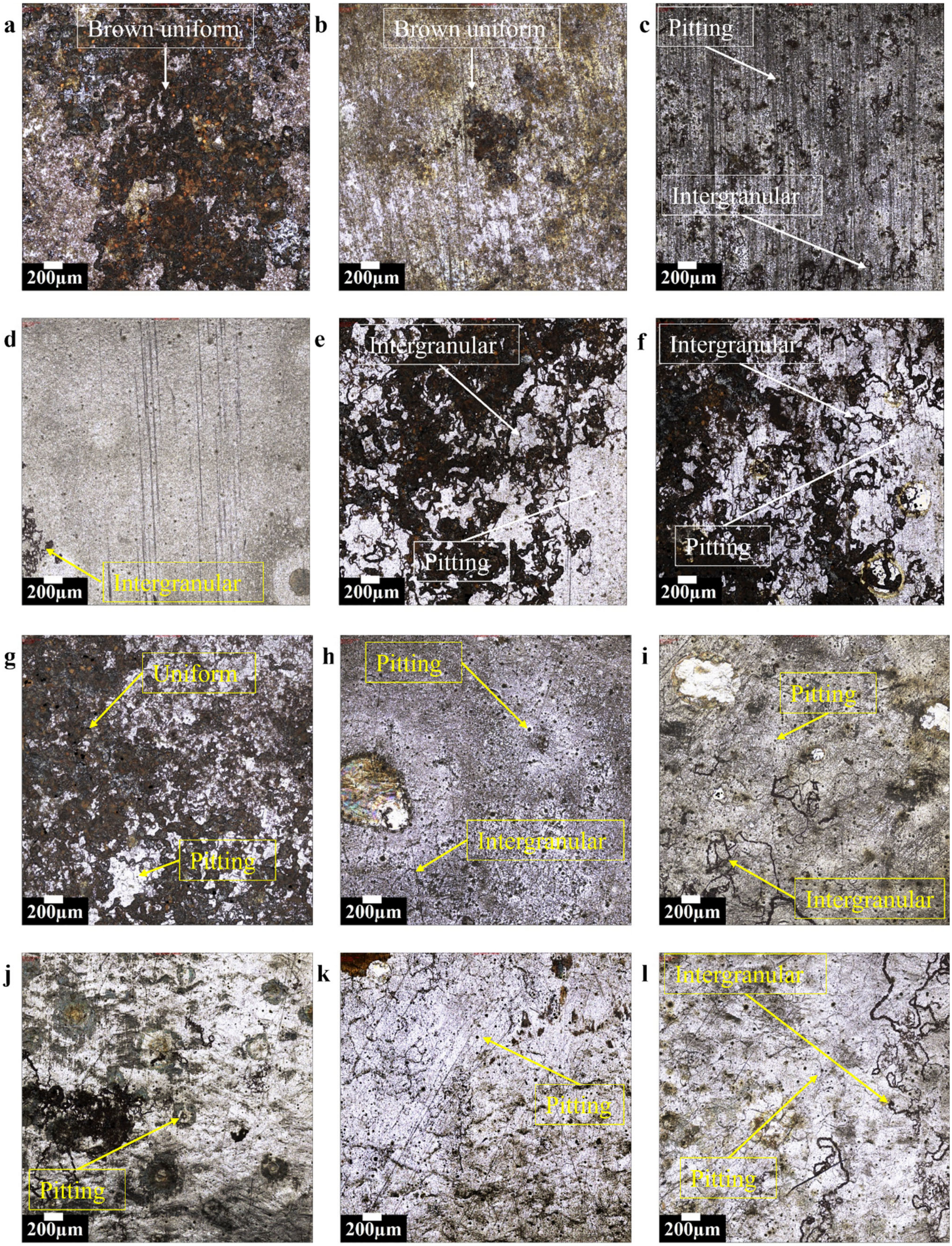

Fig. 9 Surface morphology of corroded samples; **a** OC4, **b** OC7, **c** OC10, **d** OS4, **e** OS7, **f** OS10, **g** TC4, **h** TC7, **i** TC10,**j** TS4, **k** TS7, **l** TS10

Table 5 Roughness data from Alicona infinite focus after corrosion testing

	S_a µm	S_p µm	S_v µm	S_z µm		V_{mp} ml/m^2	V_{mc} ml/m^2	V_{vc} ml/m^2	V_{vv} ml/m^2
O	3.05	19.97	20.99	23.97	O	0.11	2.60	2.88	0.23
T	3.82	23.60	22.66	26.26	T	0.12	2.10	2.68	0.27
OC4	13.51	88.08	72.28	160.36	OC4	0.81	14.50	20.81	1.19
OC7	13.31	69.07	50.92	119.99	OC7	0.47	14.37	22.84	1.09
OC10	6.03	47.10	26.90	74.11	OC10	0.21	6.86	9.90	0.54
OS4	6.85	88.60	68.04	138.80	OS4	0.45	7.15	10.87	1.94
OS7	6.49	34.31	50.19	102.35	OS7	0.38	6.19	8.26	1.01
OS10	5.24	32.59	47.87	80.46	OS10	0.23	5.62	6.90	0.80
TC4	9.65	73.87	53.78	127.64	TC4	0.90	10.50	15.56	1.09
TC7	8.50	48.09	34.02	80.58	TC7	0.72	9.83	16.35	0.86
TC10	7.85	46.57	31.55	79.64	TC10	0.64	7.36	13.43	0.56
TS4	8.08	49.30	64.63	107.61	TS4	0.48	9.56	10.76	1.52
TS7	6.29	42.98	64.37	97.06	TS7	0.43	6.29	9.91	1.47
TS10	6.26	28.10	47.76	92.47	TS10	0.38	6.14	8.76	1.23

properties of all samples studied. In addition to the aforementioned factors, the surface roughness of the metal also plays a significant role in pitting potential, general corrosion, and nucleation of pitting. Material loss takes place through electrochemical reactions during corrosion. Surface grinding typically removes surface imperfections, internal tensions, plastic distortions, micro-strains, and, possibly, alterations in the material's heterogeneity due to the fragmentation of its grains. The impact of these modifications on acid corrosion rates could surpass the impact of surface roughness [50, 51].

The tempering had not resulted in many changes in the surface roughness in terms of both surface area and volume. After corrosion, the surface roughness significantly increased, as given in Fig. 4, indicating the formation of pits or intergranular grooves on the surface of the material. OC4 showed the highest volumetric and surface area roughness, showing its high CR and formation of uniform corrosion products. OS10 showed the lowest roughness indicators, along with its low CR. The surface roughness values were related to the pH of the samples. In all the samples studied, both in chloride and sulfate media, S_a seems to decrease with an increase in pH. In all the samples, the S_a values were the lowest for pH 10 and the highest for pH 4. The corrosion rate generally increases in the same order. It is inferred that the formation of corrosion products, intergranular channels, and pits increases the surface roughness [52]. However, no direct relationships are established between corrosion rate and surface roughness.

3.5 Raman Spectroscopy

Raman spectroscopy was used after the electrochemical studies to analyze corrosion products formed. The surface analyzed was given as microscopic images, given in Fig. S2. Similar to Fig. 9, the formation of different corrosion products and different corrosion mechanisms like intergranular, uniform and pitting corrosion are observed. Raman spectra of the corrosion products are shown in Fig. 10(a–d). It is seen that the corrosion products are majorly composed of different types of oxides and oxyhydroxides. The presence of hematite (α-Fe_2O_3), wustite (FeO), magnetite (Fe_3O_4), goethite (α-FeOOH), and lepidocrocite (γ-FeOOH) are observed in the Fig. 10 depending on the medium of corrosion [53–57]. Minor shoulder peaks of wustite and magnetite are observed at 599 cm^{-1} and 655 cm^{-1}. Low to medium intensity peaks are observed at 396 cm^{-1} and 489^{-1} cm by lepidocrite and goethite. Sharp peaks at 217 cm^{-1}, 285 cm^{-1}, and 1299 cm^{-1} show hematite.

For all six samples in sulfate media (OS4, OS7, OS10, TS4, TS7, TS10) samples, sharp hematite peaks at 214 cm^{-1} and 274 cm^{-1}, and mild hematite peaks were observed at 1300 cm^{-1}. Mild peaks of lepidocrocite, goethite, and wustite were observed at 389 cm^{-1}, 485 cm^{-1}, and 585 cm^{-1}. The peaks also showed similar intensity. Broad peaks of hematite (bands at 222 cm^{-1}, 284 cm^{-1},1305 cm^{-1}, and 1578 cm^{-1}) were observed for tempered and original samples in NaCl solution (OC4, OC7, OC10, TC4, TC7, TC10). Weaker peaks of goethite (bands at 394 cm^{-1} and 485 cm^{-1}) and shoulder peaks of wustite and magnetite (bands at 598 cm^{-1} and 651 cm^{-1}) were observed in all samples. The formation of these corrosion products was from the

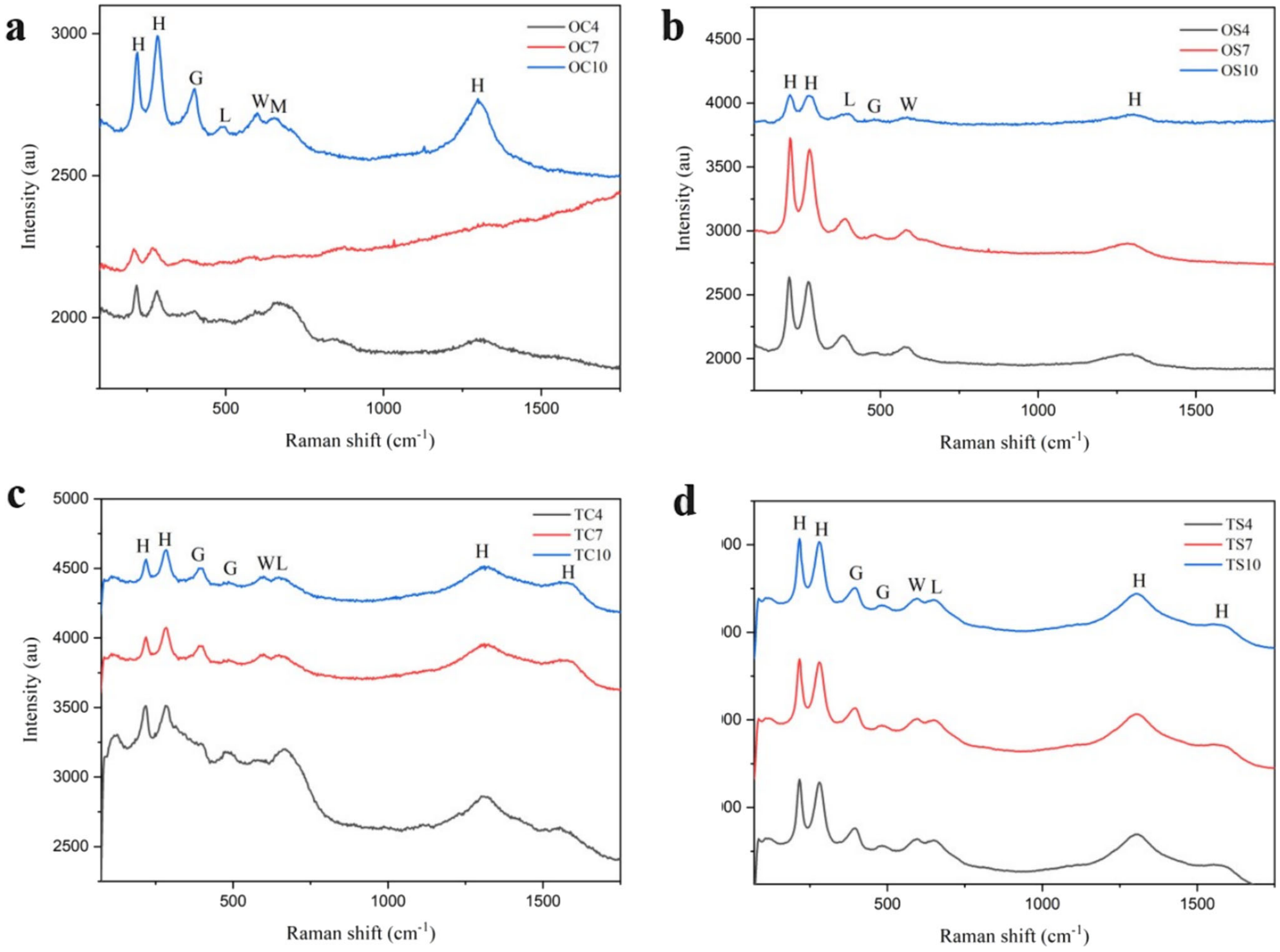

Fig. 10 Raman spectra of original (*O*) and tempered (*T*) samples at pH 4, 7, and 10; **a** and **b** *O* samples in chloride and sulfate environment, **c** and **d** T samples in chloride and sulfate environment

basic anodic and cathodic reactions that occur in an electrochemical cell. In the case of metals and alloys, it is quite well known that the anodic reaction is the dissolution of iron, as given in Eq. (4), and the cathodic reaction is the hydrogen evolution for acidic media (Eq. 5) and oxygen reduction for near neutral and basic media (Eq. 6).

$$Fe \rightarrow Fe^{2+} + 2e^{-} \tag{4}$$

$$2H^{+} + 2e^{-} \rightarrow H_2 \tag{5}$$

$$O_2 + 2H_2O + 4e^{-} \rightarrow 4OH^{-} \tag{6}$$

In this case, as the electrochemical cell includes NaCl and Na_2SO_4, the presence of Cl^- and SO_4^{2-} anions that accelerates the corrosion reaction allows the diffused Fe to form the corrosion products, as given in Eqs. 7 and 8 [58, 59].

$$Fe + 2Cl^{-} \rightarrow FeCl_2 + 2e^{-} \tag{7}$$

$$2Fe + SO_4^{2-} \rightarrow FeSO_4 + 2e^{-} \tag{8}$$

The formed corrosion products given in Eqs. 7 and 8 are unstable, which then be oxidized to form oxyhydroxides, as in Eqs. (9)–(11).

$$4FeCl_2 + 8OH^{-} + O_2 \rightarrow 4FeOOH + 8Cl^{-} + 2H_2O \tag{9}$$

$$4FeSO_4 + 8OH^{-} + O_2 \rightarrow 4FeOOH + 4SO_4^{2-} + 2H_2O \tag{10}$$

The formed oxyhydroxides in Eqs. 9 and 10 are goethite and lepidocrocite.

$$2FeOOH \rightarrow Fe_2O_3 + H_2O \tag{11}$$

However, from the Raman spectra, the corrosion product by wustite, goethite, and lepidocrocite has less intensity compared to the hematite observed. This is reasonably accepted by researchers that the initial product of corrosion are the oxyhydroxides [60, 61], which then later gets transformed to a much stable hematite by the reduction or dehydration of oxyhydroxides as shown in Eq. 11 [55]. The formation of wustite might be during the transformation of unstable oxyhydroxides to more stable forms [62, 63].

4 Conclusion

The corrosion behavior of U-bend, heat-treated S275 mild steel samples was analyzed in the study. Based on the results of this study, following conclusions are drawn.

- The samples underwent quenching at 1000 °C followed by tempering, followed by U-bending using a jig and mandrel setup. The heat treatment process transformed the austenite-ferrite microstructure in the original samples into martensite, granular bainitic ferrite, bainite and ferrite. Heat treatment resulted in decreased ductility and increased tensile strength of the samples. Fracture surface analysis after tensile testing also complemented the above results by exhibiting a uniform dimple pattern for original samples and cleavage-like fracture with non-uniform dimples for tempered samples.
- Corrosion studies were conducted using electrochemical methods in chloride and sulfate environments at pH 4, 7, and 10. The tempered and original samples exhibited significantly higher corrosion rates in acidic sulfate electrolyte solution than other samples. This heightened corrosion rate was attributed to the attack of reactive chloride and sulfate on the stress-induced cracks on the sample surface in highly acidic media.
- Microscopic analysis confirmed the occurrence of pitting, uniform, and intergranular corrosion mechanisms in the samples, dependent on the electrolyte's pH and media.
- Raman analysis was performed to identify corrosion products, with hematite being the major corrosion product.
- Roughness studies verified that the original sample had the lowest corrosion rate in sulfate media within an alkaline environment. Lower corrosion products and fewer pits led to a smoother corroded surface in the original sample.
- The presence of oxidative species on the bends can significantly increase corrosion, necessitating mitigation strategies to prevent further damage.
- Heat treatment parameters help reduce stress-induced cracks, which are key contributors to corrosion in steel structures. By refining the microstructure, the material becomes more resistant to crack propagation in corrosive environments. In our future research, the application of protective coating and inhibitors will be addressed, focusing on their ability to shield from aggressive chloride and sulfate media.

Supplementary Information The online version contains supplementary material available at https://doi.org/10.1007/s13369-025-10177-y.

Funding This research received no external funding.

Data Availability The data presented in this study are available on request from the corresponding author.

Declarations

Conflict of interest The authors declare that they have no conflict of interest.

References

1. Behera, P.K., et al.: Room temperature columnar liquid crystalline perylene bisimide as a novel corrosion resistant surface film for mild steel surface. J. Bio- Tribo-Corros. **9**(1), 18 (2023)
2. Hegazy, M.; El-Etre, A.; El-Shafaie, M.; Berry, K.: Novel cationic surfactants for corrosion inhibition of carbon steel pipelines in oil and gas wells applications. J. Mol. Liq. **214**, 347–356 (2016)
3. Bhargava, A.; Sharma, C.: Mechanical Behaviour and Testing of Materials. PHI Learning Pvt. Ltd., Delhi, India (2011)
4. Cardarelli, F.: Soils and fertilizers. Materials Handbook: A Concise Desktop Reference, pp. 927–966 (2008)
5. Parapurath, S.; Ravikumar, A.; Vahdati, N.; Shiryayev, O.: Effect of magnetic field on the corrosion of API-5L-X65 steel using electrochemical methods in a flow loop. Appl. Sci. **11**(19), 9329 (2021)
6. Muthamma, K.; Kumari, P.; Lavanya, M.; Rao, S.A.: Corrosion inhibition of mild steel in acidic media by N-[(3, 4-Dimethoxyphenyl) Methyleneamino]-4-Hydroxy-Benzamide. J. Bio- Tribo-Corros. **7**, 1–19 (2021)
7. Neto, M.Q.; Rainforth, W.M.: Effect of potential and microstructure on the tribocorrosion behaviour of beta and near beta Ti alloys II. J. Bio- Tribo-Corros. **7**, 1–12 (2021)
8. Gassama, D.; Diagne, A.A.; Yade, I.; Fall, M.; Faty, S.: Investigations on the corrosion of constructional steels in different aqueous and simulated atmospheric environments. Bull. Chem. Soc. Ethiop. **29**(2), 299–310 (2015)
9. He, Y.; Tian, G.; Zhang, H.; Alamin, M.; Simm, A.; Jackson, P.: Steel corrosion characterization using pulsed eddy current systems. IEEE Sens. J. **12**(6), 2113–2120 (2012)
10. Ding, S.; Tian, G.; Zhu, J.; Chen, X.; Wang, Y.; Chen, Y.: Characterisation and evaluation of paint-coated marine corrosion in carbon steel using eddy current pulsed thermography. NDT E Int. **130**, 102678 (2022)
11. Zhang, H.; Yunze, H.; Song, Y.; Ruikun, W.; Wenhui, C.; Maozi, L.: Exposed corrosion progression characterisation using pulsed eddy current sensing and laser profilometry. In 2019 Far East NDT

New Technology & Application Forum (FENDT), IEEE, pp. 16–20 (2019)

12. Prabhu, D.; Jilna Jomy, R.; Prabhu, P.: Influence of different heat treatment temperatures on the microstructure and corrosion behaviour of dual-phase EN8 steel in 0.5 M sulphuric acid solution. J. Bio- Tribo-Corros. (2022). https://doi.org/10.1007/s40735-022-00689-7
13. Silva, D.D., et al.: The effect of microstructural changes on mechanical and electrochemical corrosion properties of duplex stainless steel aged for short periods. Materials **13**(23), 5511 (2020)
14. Isfahany, A.N.; Saghafian, H.; Borhani, G.: The effect of heat treatment on mechanical properties and corrosion behavior of AISI420 martensitic stainless steel. J. Alloy. Compd. **509**(9), 3931–3936 (2011)
15. Majumdar, J.D.; Galun, R.; Mordike, B.; Manna, I.: Effect of laser surface melting on corrosion and wear resistance of a commercial magnesium alloy. Mater. Sci. Eng. A **361**(1–2), 119–129 (2003)
16. Amezhnov, A., et al.: Effect of chemical composition and microstructure parameters on carbon and low-alloy steel corrosion resistance under oil industry pipeline operation conditions. Metallurgist **62**(9–10), 1030–1038 (2019)
17. Parapurath, S.; Jacob, L.; Gunister, E.; Vahdati, N.: Effect of microstructure on electrochemical properties of the EN S275 mild steel under chlorine-rich and chlorine-free media at different pHs. Metals **12**(8), 1386 (2022). https://doi.org/10.3390/met12081386
18. Gupta, K.K.; Haratian, S.; Mishin, O.V.; Ambat, R.: CO_2 corrosion resistance of low-alloy steel tempered at different temperatures. Corros. Sci. **232**, 112027 (2024)
19. Ren, Y.; Cheng, X.; Li, W.; Wang, Q.; Zeng, F.: Effect of tempering temperature on stress corrosion resistance of a low alloy high strength steel with high vanadium content. Mater Today Commun **39**, 108730 (2024)
20. Wang, X.; Liang, X.; Tong, S.; Sun, X.: Influence of tempering temperature on microstructure and stress corrosion crack (SCC) behavior of a new high strength round-link chain steel. Corros. Sci., p. 112770 (2025)
21. Sheng, J.; Xia, J.; Chang, H.: Bending behavior of corroded H-shaped steel beam in underground environment. Appl. Sci. **11**(3), 938 (2021)
22. Łabanowski, J.; Świerczyńska, A.; Topolska, S.: Effect of microstructure on mechanical properties and corrosion resistance of 2205 duplex stainless steel. Pol. Marit. Res. **4**, 108–112 (2014)
23. Jacob, L.; Prasanna, K.; Vengatesan, M.; Santhoshkumar, P.; Lee, C.W.; Mittal, V.: Binary Cu/ZnO decorated graphene nanocomposites as an efficient anode for lithium ion batteries. J. Ind. Eng. Chem. **59**, 108–114 (2018)
24. Guo, D.; Li, M.; Joseph, J.; Wren, J.: A new method for corrosion current measurement: the dual-electrochemical cell (DEC). J. Electrochem. Soc. **167**(11), 111505 (2020)
25. Fernández Tavitas, R.J.; Garcés, R.S.; López Cortéz, V.H.: Hybrid laser–arc welding applied in longitudinal joints for hydrocarbon conduction pipes. MRS Online Proceed. Libr. **1766**(1), 45–52 (2015)
26. Lee, S.G.; Kim, B.; Kim, W.G.; Um, K.-K.; Lee, S.: Effects of Mo addition on crack tip opening displacement (CTOD) in heat affected zones (HAZs) of high-strength low-alloy (HSLA) steels. Sci. Rep. **9**(1), 1–12 (2019)
27. Varanasi, S.S.; More, V.M.R.; Rao, M.B.V.; Alli, S.R.; Tangudu, A.K.; Santanu, D.: Recycling ladle furnace slag as flux in steelmaking: a review. J. Sustain. Metall. **5**(4), 449–462 (2019). https://doi.org/10.1007/s40831-019-00243-9
28. Shiozawa, K.; Morii, Y.; Nishino, S.; Lu, L.: Subsurface crack initiation and propagation mechanism in high-strength steel in a very high cycle fatigue regime. Int. J. Fatigue **28**(11), 1521–1532 (2006)
29. Chen, J.; Li, X.; Han, X.: Hot stamping. In: Comprehensive Materials Processing, pp. 351–370. Elsevier (2014)
30. Katiyar, P.K.; Misra, S.; Mondal, K.: Comparative corrosion behavior of five microstructures (pearlite, bainite, spheroidized, martensite, and tempered martensite) made from a high carbon steel. Metall. Mater. Trans. A **50**(3), 1489–1501 (2019). https://doi.org/10.1007/s11661-018-5086-1
31. Wang, C.; Ding, H.; Cai, M.; Rolfe, B.: Characterization of microstructures and tensile properties of TRIP-aided steels with different matrix microstructure. Mater. Sci. Eng. A **610**, 65–75 (2014)
32. Xie, Z.; Ren, Y.; Zhou, W.; Yang, J.; Shang, C.; Misra, R.: Stability of retained austenite in multi-phase microstructure during austempering and its effect on the ductility of a low carbon steel. Mater. Sci. Eng. A **603**, 69–75 (2014)
33. Hayat, F.; Uzun, H.: Effect of heat treatment on microstructure, mechanical properties and fracture behaviour of ship and dual phase steels. J. Iron. Steel Res. Int. **18**(8), 65–72 (2011)
34. Ahsan, M.R., et al.: Heat-treatment effects on a bimetallic additively-manufactured structure (BAMS) of the low-carbon steel and austenitic-stainless steel. Addit. Manuf. **32**, 101036 (2020)
35. Awad, M.I.: Eco friendly corrosion inhibitors: inhibitive action of quinine for corrosion of low carbon steel in 1 m HCl. J. Appl. Electrochem. **36**(10), 1163–1168 (2006)
36. Sadowski, L.: Non-destructive investigation of corrosion current density in steel reinforced concrete by artificial neural networks. Arch. Civil Mech. Eng. **13**(1), 104–111 (2013)
37. Parancheerivilakkathil, M.S.; Parapurath, S.; Ainane, S.; Yap, Y.F.; Rostron, P.: Flow velocity and sand loading effect on erosion-corrosion during liquid-solid impingement on mild steel. Appl. Sci. **12**(5), 2530 (2022)
38. Kappes, M.A.: Localized corrosion and stress corrosion cracking of stainless steels in halides other than chlorides solutions: a review. Corros. Rev. **38**(1), 1–24 (2020)
39. Roy, J.J.; Cao, B.; Madhavi, S.: A review on the recycling of spent lithium-ion batteries (LIBs) by the bioleaching approach. Chemosphere **282**, 130944 (2021). https://doi.org/10.1016/j.chemosphere.2021.130944
40. Prawoto, Y.; Ibrahim, K.; Wan Nik, W.: Effect of pH and chloride concentration on the corrosion of duplex stainless steel. Arab. J. Sci. Eng. **34**(2), 115 (2009)
41. Oldfield, J.; Todd, B.: Room temperature stress corrosion cracking of stainless steels in indoor swimming pool atmospheres. Br. Corros. J. **26**(3), 173–182 (1991)
42. Alvarez, R.B., et al.: Corrosion relationships as a function of time and surface roughness on a structural AE44 magnesium alloy. Corros. Sci. **52**(5), 1635–1648 (2010)
43. Reddy, B.; Ramamoorthy, B.; Nair, P.: Surface integrity aspects and their influence on corrosion behaviour of ground surfaces. J. Instit. Eng. India Part PE Prod. Eng. Div. **86**, 35 (2005)
44. Ruther, W.; Soppet, W.; Ayrault, G.; Kassner, T.: Effect of sulfuric acid, oxygen, and hydrogen in high temperature water on stress corrosion cracking of sensitized AISI 304 stainless steel. Corrosion **40**(10), 518–527 (1984)
45. Rammelt, U.; Koehler, S.; Reinhard, G.: Synergistic effect of benzoate and benzotriazole on passivation of mild steel. Corros. Sci. **50**(6), 1659–1663 (2008)
46. Chan-Rosado, G.; Pech-Canul, M.: Influence of native oxide film age on the passivation of carbon steel in neutral aqueous solutions with a dicarboxylic acid. Corros. Sci. **153**, 19–31 (2019)
47. Mundra, S.; Provis, J.L.: Mechanisms of passivation and chloride-induced corrosion of mild steel in sulfide-containing alkaline solutions. J. Mater. Sci. **56**(26), 14783–14802 (2021)
48. Al-rubaiey, S.I.; Anoon, E.A.; Hanoon, M.M.: The influence of microstructure on the corrosion rate of carbon steels. Eng. Technol. J. **31**(10), 1825–1836 (2013)

49. Villavicencio, J.; Ulloa, N.; Lozada, L.; Moreno, M.; Castro, L.: The role of non-metallic Al_2O_3 inclusions, heat treatments and microstructure on the corrosion resistance of an API 5L X42 steel. J. Market. Res. **9**(3), 5894–5911 (2020)
50. Evgeny, B.; Hughes, T.; Eskin, D.: Effect of surface roughness on corrosion behaviour of low carbon steel in inhibited 4 M hydrochloric acid under laminar and turbulent flow conditions. Corros. Sci.. Sci. **103**, 196–205 (2016). https://doi.org/10.1016/j.corsci.2015.11.019
51. Parapurath, S.; Elkhodbia, M.; Gunister, E.: Effect of grinding, polishing and HCl on surface roughness of low carbon steel. In: 2019 Advances in Science and Engineering Technology International Conferences (ASET), IEEE, pp. 1–5 (2019)
52. Toloei, A.; Stoilov, V.; Northwood, D.: Simultaneous effect of surface roughness and passivity on corrosion resistance of metals. WIT Trans. Eng. Sci. **90**, 355–367 (2015)
53. Hazan, E.; Sadia, Y.; Gelbstein, Y.: Characterization of AISI 4340 corrosion products using Raman spectroscopy. Corros. Sci. **74**, 414–418 (2013)
54. De la Fuente, D.; Alcántara, J.; Chico, B.; Díaz, I.; Jiménez, J.; Morcillo, M.: Characterisation of rust surfaces formed on mild steel exposed to marine atmospheres using XRD and SEM/micro-Raman techniques. Corros. Sci. **110**, 253–264 (2016)
55. Zhang, X.; Xiao, K.; Dong, C.; Wu, J.; Li, X.; Huang, Y.: In situ Raman spectroscopy study of corrosion products on the surface of carbon steel in solution containing Cl^- and SO42. Eng. Fail. Anal. **18**(8), 1981–1989 (2011)
56. Sherif, E.-S.M.; Erasmus, R.; Comins, J.: In situ Raman spectroscopy and electrochemical techniques for studying corrosion and corrosion inhibition of iron in sodium chloride solutions. Electrochim. Acta **55**(11), 3657–3663 (2010)
57. Hanesch, M.: Raman spectroscopy of iron oxides and (oxy) hydroxides at low laser power and possible applications in environmental magnetic studies. Geophys. J. Int. **177**(3), 941–948 (2009)
58. Arzola, S.; Palomar-Pardavé, M.E.; Genesca, J.: Effect of resistivity on the corrosion mechanism of mild steel in sodium sulfate solutions. J. Appl. Electrochem. **33**(12), 1233–1237 (2003). https://doi.org/10.1023/B:JACH.0000003855.95788.12
59. Hasan, B.O.; Sadek, S.A.: Corrosion behavior of carbon steel in oxygenated sodium sulphate solution under different operating conditions. Adv. Chem. Eng. Res. **2**(3), 61–71 (2013)
60. Majzlan, J.; Mazeina, L.; Navrotsky, A.: Enthalpy of water adsorption and surface enthalpy of lepidocrocite (γ-FeOOH). Geochim. Cosmochim. Acta **71**(3), 615–623 (2007)
61. Nie, X.; Li, X.; Du, C.; Huang, Y.; Du, H.: Characterization of corrosion products formed on the surface of carbon steel by Raman spectroscopy. J. Raman Spectrosc. **40**(1), 76–79 (2009)
62. Alaoui Mouayd, A.; Orazem, M.E.; Sutter, E.M.M.; Tribollet, B.; Koltsov, A.: Contribution of electrochemical dissolution during pickling of low carbon steel in acidic solutions. Corros. Sci. **82**, 362–368 (2014). https://doi.org/10.1016/j.corsci.2014.01.036
63. Demoulin, A.; Trigance, C.; Neff, D.; Foy, E.; Dillmann, P.; L'Hostis, V.: The evolution of the corrosion of iron in hydraulic binders analysed from 46- and 260-year-old buildings. Corros. Sci. **52**(10), 3168–3179 (2010). https://doi.org/10.1016/j.corsci.2010.05.019